

Vortex-Induced Vibration on a Spring-Mounted Cylinder

Linear and Non-Linear Analysis

Diogo Ferreira Sabino
diogo.sabino@tecnico.ulisboa.pt

Instituto Superior Técnico, Universidade de Lisboa, Portugal

December 2018

Abstract

The vortex-induced vibration of a spring-mounted, rigid circular cylinder, immersed in a Newtonian viscous incompressible flow and allowed to move in the direction orthogonal to the unperturbed flow is investigated in the low Reynolds regime ($15 \leq Re \leq 60$) by the means of a global linear and non-linear analysis. The motion is either sinusoidally imposed or governed by a model equation of the free motion. The results for the linear forced-case are described in terms of impedance (ratio between the vertical force coefficient and the cylinder velocity) and compared with a Direct Time Integration, yielding a good match. A detailed investigation allowed to identify three thresholds, associated to the energy transfer between the cylinder and the fluid and to the onset of the vortex-shedding. A theoretical argument, based on asymptotic developments, is introduced in order to rate the forced and free problems and to provide a stability criterion in terms of impedance. Regarding the freely moving cylinder, results are obtained with a linear stability analysis, predicting the steady state stability as function of the free motion parameters (Re, m^*, U^*, γ). On the other hand, the non-linear analysis is firstly carried out for the fixed-case cylinder, based on a weakly non-linear and a self-consistent approaches and compared with the more recent literature. A new approach towards the characterisation of the limit cycle, a harmonic balance technique, is proposed, leading to shorter computation times and more accuracy than the former ones. A theoretical extension of the harmonic balance method is presented for the free-case cylinder.

Keywords: vortex-induced vibrations, spring-mounted cylinder, global stability analysis, parametric instability, harmonic balance approach.

1. Introduction

Flows over *bluff bodies* are often encountered in a natural environment as well as in many engineering applications. The flow around a cylinder has been considered as a benchmark study for more than a century, as a canonical example of a bluff body. The simplicity of the cylinder case enables the researchers to understand the fundamental concepts associated with such apparatus and eventually to extrapolate to more complex geometries. Depending on the circumstances, the fluid may exhibit a massive flow separation and a *vortex shedding* phenomenon, known as the von-Kármán street.

One of the consequences of this phenomenon is the dramatic increase of the drag force, due to the low base pressure on the rearward of the body. Concomitantly, the unsteadiness emerging in wake may excite resonant structural vibrations, thus causing fatigue failure, early deterioration of the materials and consequent safety problems. Such vibrations came from the fluctuations in the lift and drag forces acting on the body surfaces. Consequently, the coupling between the structure and the flow, commonly

referred as *fluid-structure interaction* or *flow-induced vibration*, must be taken into account when studying these phenomena, in order to fully understand such configuration. In particular, when the coupling has its origin directly on the flow, endowing the cylinder with a resonance behaviour at the same frequency as the shedding, it is referred as *vortex-induced vibration* (VIV).

All these features are fundamentally linked to instability mechanisms, arising above a certain critical Reynolds number, Re_c . Thus, a deeper understanding on these instabilities and their accurate prediction, as well as their control, could be of great importance, not only in the context of basic research but, also from an industrial point of view.

The present study is framed in the thematic of hydrodynamic instabilities, with the focus made on the characterisation of the flow behaviour, by a linear and non-linear global stability approach, at a Reynolds number, Re , near the bifurcation, where the flow transits from a steady equilibrium state to an unsteady periodic state. For the fixed-case cylinder, where no VIV is taken into account, such

phenomenon is already well documented in the literature, occurring around $Re_c \approx 47$ [1]. However, when the cylinder displacement is allowed, introducing an additional degree of freedom, the symmetry breaking is expected to arrive at earlier Re and possibly triggered by a different mechanism from the classical one encountered in the fixed-case cylinder. These analyses were made possible by allowing the cylinder to move in the direction orthogonal to the incoming flow, either by a free or an imposed motion. Further, a link between these two cases appears when their growth rates tends to zero. This enables to predict the different characteristics associated to the free-case, with the help of an asymptotic expansion, based on the results of the forced-case.

Different linear and non-linear approaches were already presented in the literature. Concerning the Linear Stability Approach (LSA) carried out, the present study follows the investigations made by [2], [3], [4] and [5], where the Re_c was showed to decrease to less than a half of the Re_c associated to the fixed-case cylinder, depending on the mass ratio m^* , the reduced velocity U^* and the damping factor γ . These parameters are associated to the cylinder free motion equation and are discussed later.

Concerning the non-linear approach, used for the regimes at $Re > Re_c$, the state of the art studies were interested either in characterising the transition to a limit cycle, i.e. the fully developed periodic flow, or in characterising the limit cycle itself. Such objectives were achieved in a first instance for the fixed-cylinder by [6], using an *Weakly Non-Linear* (WNL) approach, and subsequently by [7], using a *Self-Consistent* (SC) approach. The present non-linear study is concentrated in the fixed-case cylinder, with a theoretical extension to the free-case and it is only interested in characterising the limit cycle. This was done by the means of a *Harmonic Balance* (HB) method. This method, based on a Fourier Series, directly characterises the limit cycle and can be truncated at the desired order, representing an advantage over other methods in terms of computation time and complexity.

2. Background

2.1. Fluid and Rigid Body Model Equations

A Cartesian reference frame, attached to the center of the cylinder, was considered, as represented in Fig. 1, with the \vec{x} -axis parallel to the flow direction. For $Re \lesssim 188$, the two-dimensional fluid flow is governed by the non-dimensional unsteady incompressible Navier–Stokes equations

$$\begin{cases} \frac{\partial \vec{u}}{\partial t} + \frac{\partial \zeta}{\partial t} \vec{y} = -(\vec{u} \cdot \vec{\nabla}) \vec{u} - \vec{\nabla} p + \frac{2}{Re} \vec{\nabla} \cdot \vec{\varepsilon}(\vec{u}), & (1a) \\ \vec{\nabla} \cdot \vec{u} = 0, & (1b) \end{cases}$$

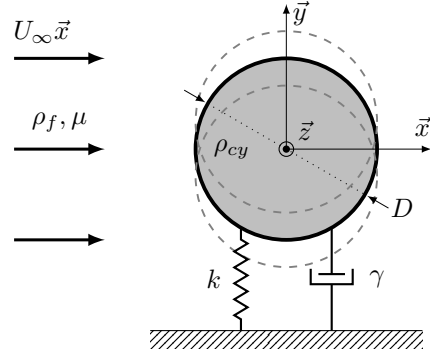


Figure 1: Spring-damping mounted cylinder diagram.

where \vec{u} and p are the fluid velocity and pressure fields, ζ is the vertical cylinder displacement and $\vec{\varepsilon}(\vec{u})$ is the strain rate tensor. The former equations were made dimensionless using the cylinder diameter D as characteristic length scale, the incoming uniform flow stream velocity U_∞ as the reference velocity and $\rho_f U_\infty^2$ as the reference pressure, where ρ_f is the fluid density. The Reynolds number is therefore defined as $Re = \rho_f D U_\infty / \mu$, where μ is the fluid dynamic viscosity. The classical boundary conditions used in these kind of problems were used to close the system. Initial condition is discussed later.

In the forced-case, the cylinder's velocity was sinusoidally imposed as $\zeta_F(t) = -|\zeta_F| \sin(\omega_F t + \theta)$, where ω_F is the imposed frequency and θ a general phase, considered to be nil. The Strouhal number can be therefore defined as $St = \omega_F D / 2\pi U_\infty$. In contrast, the cylinder's motion of the free-case problem was taking into account by a scalar linear model equation that reads:

$$\ddot{\zeta} + \frac{4\pi\gamma}{U^*} \dot{\zeta} + \left(\frac{2\pi}{U^*}\right)^2 \zeta = \frac{2C_y}{\pi m^*}, \quad (2)$$

where C_y is the vertical force coefficient felt in the cylinder surface. The latter, along with the boundary conditions imposed by the cylinder displacement on the flow, ensures the coupling between the structure and the fluid dynamics.

2.2. Energy Transfer and Impedance Concept

A key feature associated to an impedance definition is detailed next, linking the free and the forced problems. In a first time, one can define the net energy transfer from the fluid to the cylinder, over a period T , E_{cycle} , as

$$E_{cycle} = \int_0^T [C_y(t) \dot{\zeta}(t)] dt. \quad (3)$$

Noting the complex amplitude with a hat notation (e.g. $\hat{\zeta}$ for the cylinder velocity and \hat{C}_y for the vertical force coefficient), the impedance can be defined as

$$Z = -\frac{\hat{C}_y}{\hat{\zeta}}. \quad (4)$$

If one considers the forced-case motion, the energy formula degenerates into

$$E_{cycle,h} = -\pi|\hat{\zeta}|^2\omega_F Z_{r,F}, \quad (5)$$

representing a stability criterion for a harmonic motion, based on the energy transfer.

2.3. Impedance-Based Asymptotic Expansion

Based on the impedance concept, the link between the free and forced problems is made via an asymptotic expansion of Eq. (2) around $E_{cycle,h} = 0$, i.e. $\lambda_r = 0$. This implies that $Z_r \ll Z_i$ and $\lambda_r \ll \lambda_i$, arriving to a ϵ^0 and ϵ^1 order predictions. The latter was mainly used for $m^* \gg 1$. This expansion will enable to predict the free-case characteristics, otherwise found by solving an eigenvalue problem, just by solving the forced-case problem.

2.4. Linear and Non-Linear Approach

In a linear frame, the state vector solution, \vec{q} , was decomposed into a steady and a linear perturbation solutions in a form $\vec{q} = \vec{q}_b + \epsilon\vec{q}'$, where ϵ is considered a *small* parameter associated to the linear approach. When inserted in the problem's equations, a first set of equations for \vec{q}_b arise, called the baseflow equations. Regarding the linear perturbation, \vec{q}' is posed as $\vec{q}' = \Re(\hat{q}e^{(\lambda_r + i\lambda_i)t})$, where, for the free-case, \hat{q} corresponds to the eigenmode and $\lambda = \lambda_r + i\lambda_i$ to the eigenvalue. The real and imaginary parts of λ correspond to the amplification rate and angular frequency of the eigenmode, respectively. Therefore, \vec{q}' will be associated either to a forced problem, in the form of $\mathcal{A}_F\vec{q}'_F = \mathcal{F}$, or to an eigenvalue problem, in the form of $\mathcal{A}\hat{q} = \lambda\mathcal{B}\hat{q}$. The amplification rate is identically equal to zero for the forced-case problem. However, for the free-case, λ_r will define if the solution tends to vanish or linearly grows up to infinity, representing a stability criterion that can be posed as

if $\exists \lambda \in \mathbb{C} \mid \lambda_r > 0 \Rightarrow$ the solution is unstable.

In a non-linear frame, the state vector solution was decomposed into a mean and a non-linear perturbation solutions in a form $\vec{q} = \vec{q}_m + \vec{q}'$. Further, in the case of an HB approach, the perturbation is assumed to be periodic and represented by two harmonic components, $\vec{q}^{(n),c}$, $\vec{q}^{(n),s}$, characterising the non-linear fluctuations at n^{th} order and up to a frequency $n\omega$. The state vector can be therefore defined as:

$$\vec{q}(\vec{r}, t) = \vec{q}_m + \sum_{n=1}^{\infty} [\vec{q}^{(n),c} \cos(n\omega t) + \vec{q}^{(n),s} \sin(n\omega t)]. \quad (6)$$

3. Methods and Implementation

3.1. Iterative Methods

Different iterative methods were used in the present study, in order to solve the former prob-

lems. The baseflow equations were solved via a *Newton–Raphson* method. This method searches a steady solution of the current problem by decomposing it, for each iteration, into an approximative solution at the i^{th} iteration, $\vec{q}_b^{(i)}$, and a small correction associated to the next iteration, $\delta\vec{q}_b^{(i+1)}$. If the method converges, the small correction will tend to zero, whereas the iterative solution will tend to the steady solution. The same method was also used in the Harmonic Balance approach when searching for the limit cycle solution.

On the other hand, the eigenvalue problem $\mathcal{A}\hat{q} = \lambda\mathcal{B}\hat{q}$ was also solved via an iterative procedure, instead of using a classical direct method. This latter class of methods would compute the whole spectrum, being costly prohibitive and useless in the present analysis. The alternative was to use an *Arnoldi* method and search for a limited set of eigenvalues located in the vicinity of a “shift” value. Further, a particular case of this method, called *shift-and-invert* method, was implemented by searching for just one eigenvalue. During the parametric study of the eigenvalue problem, the shift value was calculated via a continuation technique based on the two previous computed eigenvalues.

3.2. Numeric Implementation

The numeric implementation was made via *FreeFem++*, a software based on a finite element method. An auxiliary set of *Matlab* programs, assembled in the a software called *StabFem*, were used and developed to more easily monitor the computations and process the results. While the *FreeFem++* codes were used to generate and adapt the meshes and to solve the various problems arising in the analysis, the *Matlab* codes were used as a wrapper and driver to monitor the computations and perform the required loops over parameters.

The variational formulation of the problem was built using $\mathcal{P}2$ (quadratic) elements for each component of the velocity and $\mathcal{P}1$ (linear) elements for the pressure, representing the classical Taylor–Hood polynomials. The computational domain was discretised via a Delaunay–Voronoi algorithm generating an unstructured triangular mesh and adapted via an automatic procedure to a given field. This adaptation relies on the AdaptMesh procedure of the *FreeFem++* software (see, for instance [8]). An adaptation to the structural sensitivity, calculated via the solutions of the direct and adjoint eigenproblems (see [9]) was used, in order to well discretise the wavemaker region in the rear of the cylinder.

4. Linear Forced-Case Results

The results for the linear forced-case, described in the following paragraphs, were treated in terms of the impedance Z_F , as function of the prescribed oscillation frequency, here represented by the St_F

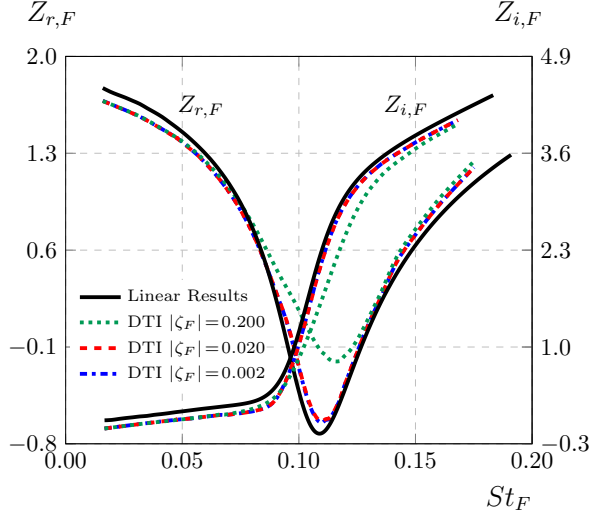


Figure 2: Linear forced-case validation with DTI: $Z_{r,F}$ and $Z_{i,F}$ variation with St_F for $Re = 25$.

number.

4.1. Validation

The validation of the present linear forced results was done with the help of a Direct Time integration (DTI). Details of the DTI simulations are presented in Chap. 3 of [10] or, more succinctly, in the associated articles of the same author. The main parameter to pay attention to is the amplitude of the imposed oscillation. The latter have to be small enough to respect the linear hypothesis and therefore be able to validate the linear forced approach. The comparison between different imposed amplitudes for the same range of St_F at $Re = 25$ is presented in Fig. 2, for $Z_{r,F}$ and $Z_{i,F}$. One can see that, as the amplitude decreases, the DTI solution approaches the linear solution. The results for the two smaller amplitudes give almost the same results, confirming that the considered displacement amplitude is small enough. Using the lowest amplitude, several DTI simulations were carried out and compared with the linear approach, achieving a good agreement, thus validating the results.

4.2. Critical Re Numbers

A general presentation of the results can be seen in Fig. 3, corresponding to four different Re computations. The results are sketched in a diagram known as the Nyquist diagram, enabling to highlight the critical points, with the real and imaginary parts of Z_F at the axis.

The first interesting phenomenon occurs at $Re_{c1} \approx 20$. Indeed, one can see that, between the curves at $Re = 15$ and $Re = 25$, there are some Re values for which $Z_{r,F}$ is negative between some frequencies. The limit condition can be formulated as

$$\text{At } Re = Re_{c1}, \exists St_F \in \mathbb{R}^+ \mid Z_{r,F}(St_F) = 0.$$

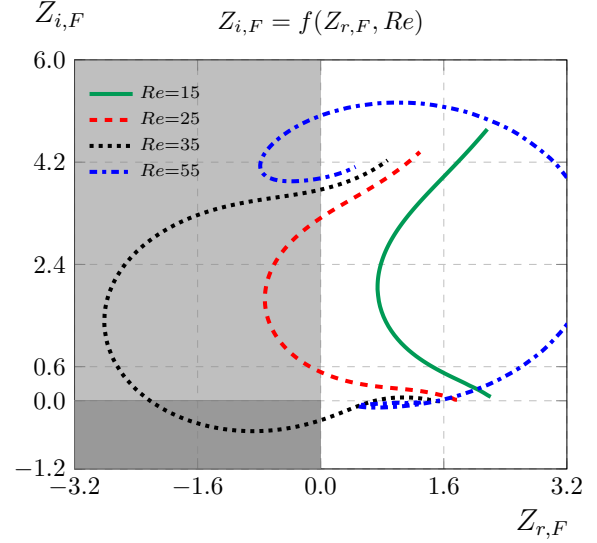


Figure 3: Nyquist diagram for Z_F as function of St for four different Re . Some branches go to infinity when crossing a critical Re . The lighter grey and dark grey regions represent the unstable zones for $Re_{c1} < Re < Re_{c3}$ and $Re_{c2} < Re < Re_{c3}$, respectively.

Having in mind the definition of Eq. (5), this condition means that, for the present Re ,

$$\exists [\vec{u}'_F(\vec{r}), p'_F(\vec{r}), |\dot{\zeta}'_F|] \mid E_{cyclo,h} = 0,$$

i.e., above the Re_{c1} , the energy transferred from the fluid to the cylinder becomes positive for some values of St_F .

The second interesting phenomenon occurs at $Re_{c2} \approx 30$. Near this Re , one observes that there is for some Re_{c2} a curve that crosses the origin for a certain value of St_F . The search for this point can be set with the condition

$$\text{At } Re = Re_{c2}, \exists St_F \in \mathbb{R}^+ \mid Z_F(St_F) = 0.$$

The third interesting phenomenon occurs at $Re_{c3} \approx 47$. Near this Re , one observes that there is for some Re_{c3} a curve that tends to infinity, i.e.

$$\text{At } Re = Re_{c3}, \exists St_F \in \mathbb{R}^+ \mid Z_F(St_F) = \infty.$$

This Re value also corresponds to Re_c for the fixed-case problem. A resume of the results is presented in Tab. 1, showing the three thresholds found, with its associated St_F , ω_F and $Z_{i,F}$ values.

Re_c	St_F	$\omega_F(\text{rad/s})$	$Z_{i,F}$
19.915	0.1040	0.6533	1.9010
30.349	0.0950	0.5973	0
46.766	0.1165	0.7323	∞

Table 1: Thresholds characteristics for the linear forced-case cylinder.

5. Linear Free-Case Results

The results for the free-case, described in the following paragraphs, were analysed in terms of the physical eigenvalues of the eigenproblem, λ , and their variation with the problem's parameters, (Re, m^*, U^*, γ) . The value of γ will be considered to be nil throughout the following analysis, with the exception of Sec. 5.8. The impedance-based predictions at order ϵ^0 can be seen throughout this section, when compared with the eigenproblem results for $\lambda_r \rightarrow 0$. Regarding the impedance-based predictions at order ϵ^1 , they are analysed in detail in Sec. 5.7.

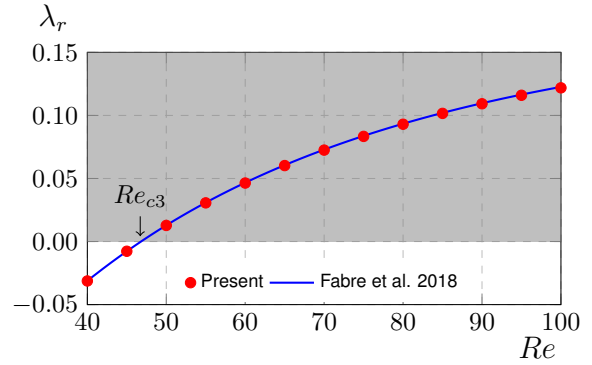
5.1. Eigenmode Classification and Behaviour

As reported in [2], [3], [5] (the latter will hereinafter be denoted as **NM16**), the free transverse cylinder motion introduces two additional complex-conjugate eigenvalues to the physical spectrum and therefore two additional eigenmodes. Contrasting with the fixed-case, where only one (fluid) mode is found, the free-case cylinder presents two eigenmodes. Their classification is divided according to their nature and relation.

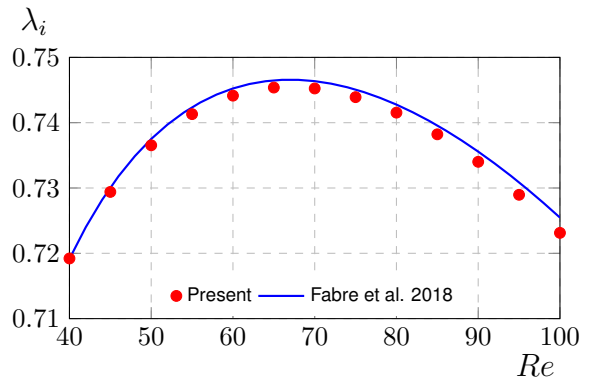
When decoupled, the eigenmodes will be referred as the fluid mode (FM) and the elastic mode (EM), as proposed in **NM16**. Their identification is based on their characteristics in the limit of very large m^* . To do so, eigenvalues are tracked over a wide range of U^* while keeping Re and m^* fixed. In general, for large values of m^* , the eigenmodes corresponding to the two leading eigenvalues exhibit a decoupled behaviour with respect to U^* . The imaginary part of the eigenvalue associated to the EM tends to the natural eigenvalue angular frequency of the cylinder-only system, i.e. $2\pi/U^* \equiv \omega_N$, whereas the eigenvalue associated to the FM tends to the leading eigenvalue computed for the flow past a stationary cylinder. However, for relatively low m^* the distinction between FM and EM is not possible, since eigenvalues may coalesce for certain combinations of (Re, U^*, m^*) , namely for lower m^* or when $Re \rightarrow 46.7$. The two leading eigenmodes do not exhibit a clear distinction in terms of their affiliation to being either a FM or an EM. They are therefore referred as coupled modes and, following **NM16** nomination, they will be denoted as fluid-elastic mode 1 (FEM1) and fluid-elastic mode 2 (FEM2). Further, for small U^* , the FEM1 resembles to the FM, whereas the FEM2 is similar to the EM. However, for large U^* , the characteristics of FEM1 and FEM2 resemble to the EM and to the FM, respectively.

5.2. Validation

The validation of the results is firstly done by comparing the results with the fixed-case cylinder. For that purpose, results are obtained for $U^* \rightarrow 0$. This asymptotic approach constrains the spring stiffness



(a) Amplification rate variation with Re .



(b) Angular frequency variation with Re .

Figure 4: Comparison between the eigenvalues from the FM for $U^* \rightarrow 0$ and from the fixed-case cylinder. Grey zone represents the unstable region ($\lambda_r > 0$).

to large values, $k \rightarrow \infty$ when m^* remains finite. It is firstly noted that the imaginary part associated to the EM tended to infinity, for all Re , as expected for the natural frequency of the structure-only system, $2\pi/U^*$. Secondly, the imaginary and real parts of the eigenvalue associated to the FM are compared with the results from the fixed-case reported in [11]. As showed in Fig. 4, a perfect match is found, for a range of $Re = [40; 100]$.

In a second time, the results are compared with data from **NM16** and from [4] (hereinafter denoted as **ZLYJ15**). Fig. 5 shows the real and imaginary parts of the eigenvalue variation along $U^* = [3, 11]$ for $Re = 60$ and $m^* = 20$. Imaginary parts are sketched in terms of $St_{LSA} = \lambda_i/2\pi$.

While the imaginary part presents no difference when comparing the present study and the cited references, the real part of the eigenvalue shows a discrepancy between all sources. Although the qualitative match of the results, their values do not seem to agree. One notes, however, that λ_r at $U^* = 3$ is close to the fixed-case cylinder value depicted in Fig. 4 for the present study, although this is not verified by the values from **NM16** or **ZLYJ15**.

It is clear that, for $Re = 60$, it will always exist an eigenvalue for which λ_r is positive, at any reduced

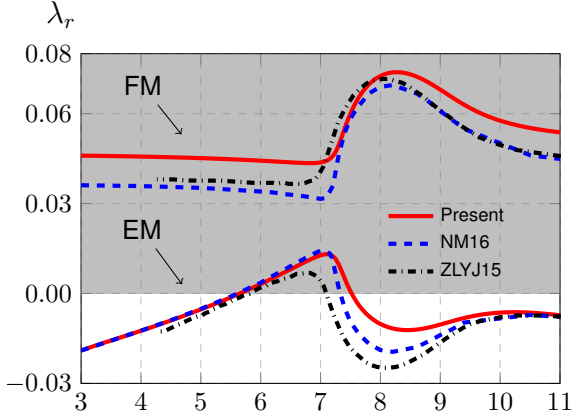
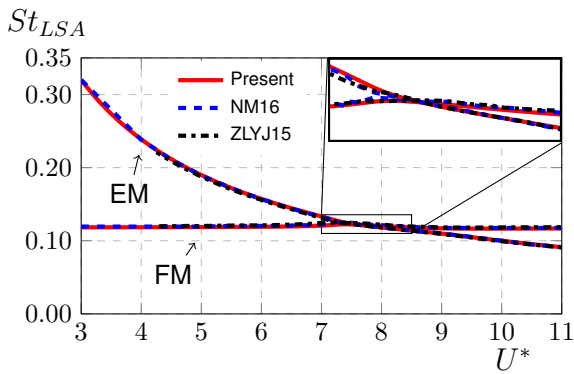

 (a) Amplification rate variation with U^* .

 (b) Angular frequency variation with U^* .

Figure 5: Real and imaginary parts of the eigenvalue variation with U^* at $Re = 60$ for $m^* = 20$. The zoom in the frequencies shows that the curves cross each other. Grey zone represents the unstable region ($\lambda_r > 0$).

velocity. For the purpose of identifying the stable and unstable zones, a different analysis, explained afterwards was carried out at lower Re values.

5.3. Instability Threshold at $Re \approx 20$

The following analysis was carried out at lower Re , fixing m^* , whereas the value of U^* was varied within a range of $U^* = [3, 11]$. For relatively low mass values, the former considerations were shifted to lower U^* values.

When decoupled, the eigenvalues associated to the FM present always a negative amplification rate. When coupled, the eigenvalues of one of the modes also obeys to the this observation (namely the FEM1). The objective is then determine for which Re the EM (or the other coupled mode, FEM2) presents an eigenvalue with a zero amplification rate and for which U^* .

Results shows that, at $Re = 19.946$, it appears the first λ_r positive in the spectrum, indicating that, below this threshold, the system is stable and above this threshold, since there is *at least* one eigenvalue with positive amplification rate, the system is lin-

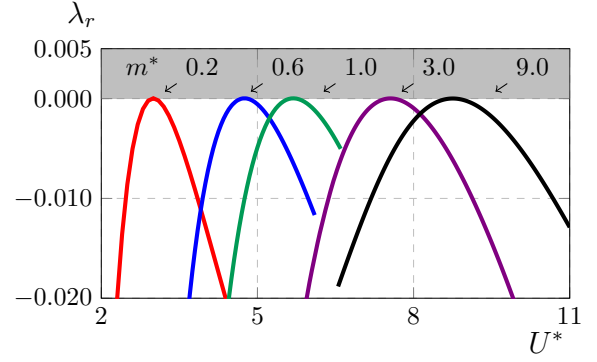
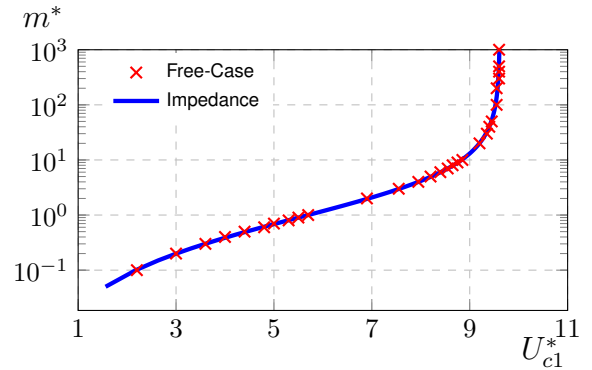

 (a) Variation of λ_r with U^* for different m^* at $Re_{c1} \approx 20$. The value of m^* is noted above curves in the graphic.

 (b) Variation of U_{c1}^* with m^* at $Re_{c1} \approx 20$.

Figure 6: Results for Re_{c1} , varying U^* (at the top) and varying m^* (at the bottom). Grey zone represents the unstable region ($\lambda_r > 0$).

early unstable. A particular value of U^* is found to be associated to this zero amplification rate and found to be dependent of the values of m^* . Nevertheless, the threshold is found always at $Re \approx 20$, for all m^* . This can be seen in Fig. 6(a), where λ_r is depicted as function of U^* for different values of m^* and at $Re = Re_{c1}$.

Furthermore, the value of U^* at the threshold, $U^*(Re_{c1}, \lambda_r = 0) \stackrel{\text{def}}{=} U_{c1}^*$, increases with the increase of the mass ratio. Its variation with m^* is compared in Fig. 6(b) with the impedance-based predictions at $\mathcal{O}(\epsilon^0)$, finding a perfect match.

5.4. Spectrum Behaviour at $20 < Re < 47$

In a regime between $20 < Re < 47$, one will obtain a stable or unstable solution, depending on the values of m^* and U^* . The results at a fixed Re , for different mass ratios, are now analysed. The spectrum for $Re = 44$ is sketched in Fig. 7. For $m^* = 1000$, the modes are clearly separated, with the EM being unstable at $U_{unst} = [6.47; 9.04]$. The FM is always stable. For a $m^* = 100$, the modes appear closer than the latter case, although remaining separated. The EM is unstable at $U_{unst} = [6.40; 9.17]$, whereas the FM is again always stable. Lastly, for a $m^* = 10$, the modes are coupled and it is the FEM2 that

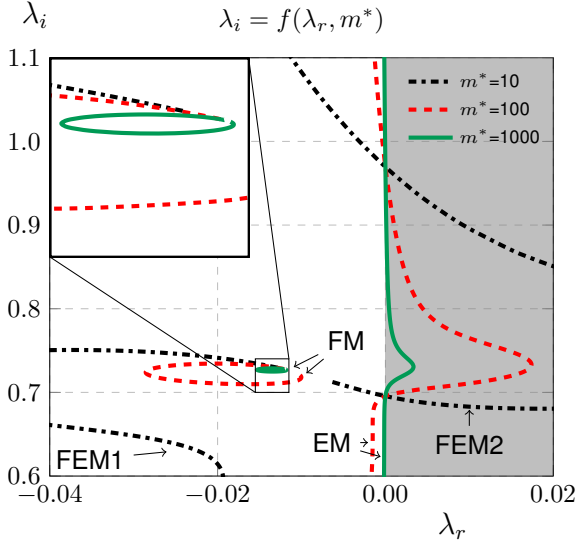


Figure 7: Spectrum for $Re = 44$ and three different values of m^* . The different nature of the eigenmodes is identified with an arrow and a legend. Grey zone represents the unstable region ($\lambda_r > 0$).

crosses the \vec{y} -axis for $U_{unst} = [5.79; 10.75]$. It was observed that, for coupled modes, is always the FEM2 that crosses the \vec{y} -axis. One also notes that the EM and the FEM2 always cross the \vec{y} -axis at the same λ_i , being unstable for $\lambda_i = [0.70; 0.97]$, whereas the U^* range, in which λ_r is positive, increases.

One can observe a high value of the amplification rate near the resonance zone ($\lambda_i \approx 0.74$). Further, this value increases as the m^* decreases, showing the evidence of a stronger coupling for lower masses.

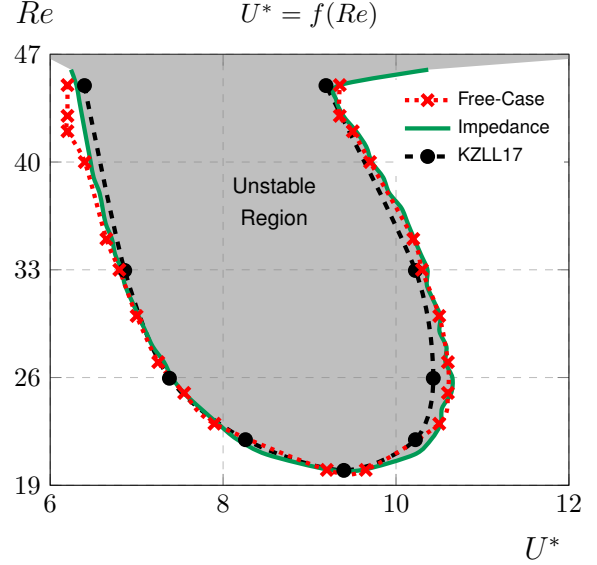
5.5. Instability Threshold at $Re \approx 47$

This paragraph aims to resume and clarify what appends at Re_{c3} . As mentioned, the nature of the modes is highly influenced by the proximity to this threshold. The critical mass ratio values of the curve that divides the $m^* - Re$ plane into two regions, coupled and uncoupled modes, tend to increase when $Re \rightarrow Re_{c3}$. For $Re > 47$, one will always find an unstable mode, either from the FM, from the EM, or from the coupled modes. Mathematically, one can state that

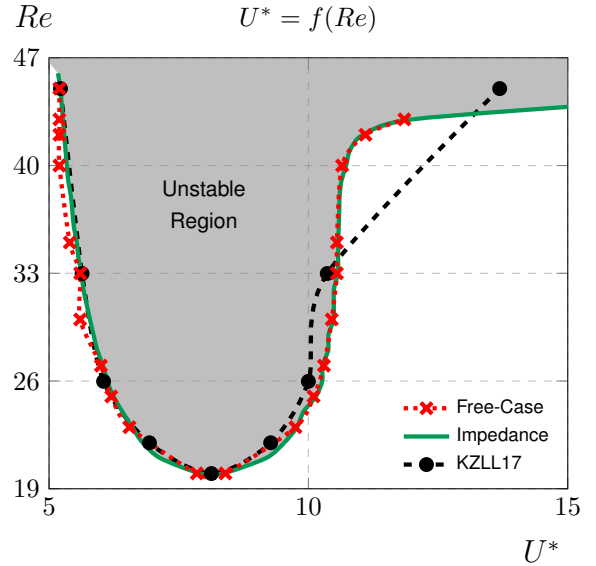
$$\text{if } Re > Re_{c3} \Rightarrow \forall U^*, m^* \in \mathbb{R}^+, \exists \hat{q} \mid \lambda_r > 0.$$

5.6. Instability Map: $Re - U^*$ Plane

From the observations made in the last paragraphs, an overall picture of the results is now presented and referred as an instability map, enabling a global vision of the problem in this Re regime. Comparisons with the impedance-based predictions at $\mathcal{O}(\epsilon^0)$ will also be plotted. The main objective of this analysis is to determine the limiting curve that separates the non-vibrational zone (stable) from the possible



(a) Results comparison for $m^* = 50$.

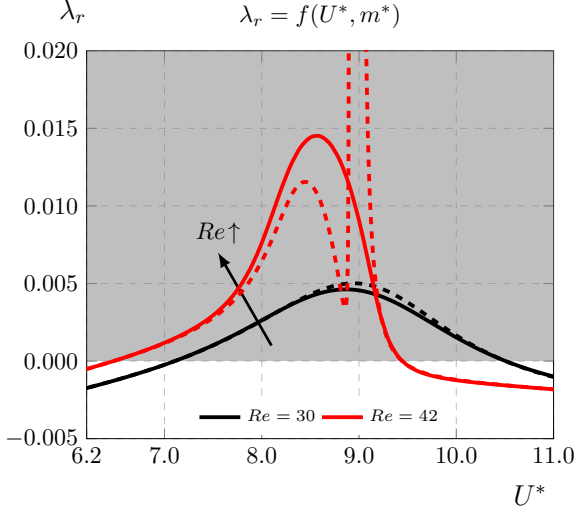


(b) Results comparison for $m^* = 4.73$.

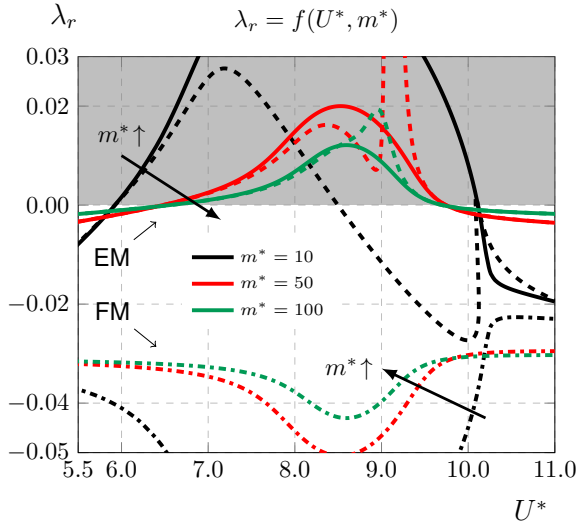
Figure 8: $Re - U^*$ plane distinguishing two zones, with the comparison between free results from the present study and from Kou et al. 2017 (KZLL17) and the 1st order impedance-based predictions. Grey zone represents the unstable region ($\lambda_r > 0$).

vibrations occurrence zone (unstable).

For that purpose, a LSA was carried out over a wide range of reduced speed U^* , for several values of Re and at a fixed m^* . The stability criterion mention before is then used to identify the stable and unstable zones, i.e. if $\lambda_r > 0$ the system is linearly unstable. The values of U^* for which $\lambda_r = 0$, for different values of Re , are plotted in a $Re - U^*$ plane. This analysis was done for $m^* = 50$ and $m^* = 4.73$ and is presented in Figs. 8(a) and 8(b), respectively. The results are compared with **KLZZ17** and the 1st order impedance-based predictions, observing a



(a) Amplification rate for the impedance predictions and LSA results for two values of Re at $m^* = 100$.



(b) Amplification rate for the impedance predictions and LSA results for three values of m^* at $Re = 40$.

Figure 9: Comparison between results from impedance predictions at ϵ^1 order and from the LSA results. The EM is represented by a solid line, whereas the FM is represented by a dash-dotted line and the impedance predictions by a dashed line. Grey zone represents the unstable region ($\lambda_r > 0$).

good agreement between results.

One may note that the unstable zone limit starts at Re_{c3} for lower U^* values and tends to a fixed value when $U^* \rightarrow \infty$. This asymptotic value tends to decrease as m^* decreases. Therefore, for high values of m^* , the curve will tend to Re_{c3} , whereas for low values of m^* , the curve is expected to tend to Re_{c2} . A similar reasoning is found in a later paragraph, where the influence of γ is investigated.

5.7. Impedance-Based Predictions at Order ϵ^1

As previously explained, the impedance-based method aims to calculate the parameter values at

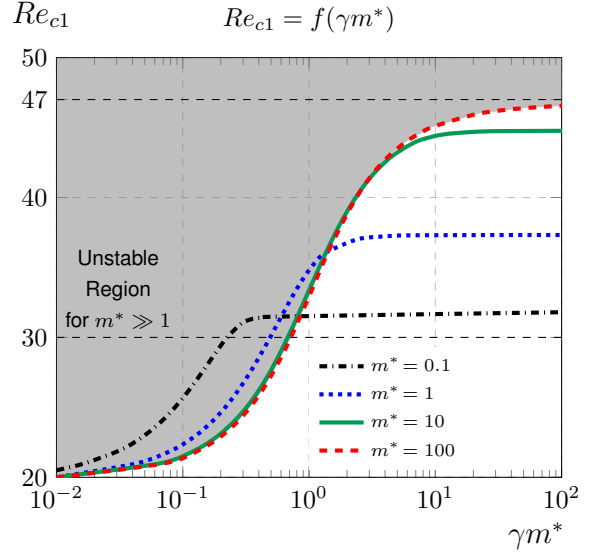


Figure 10: Variation of Re_{c1} with the product γm^* for several values of m^* . Grey zone represents the unstable region for $m^* \gg 1$. Horizontal dashed lines indicate the Re_{c2} and Re_{c3} .

which the free-case cylinder, defined as an eigenvalue problem, becomes unstable, using the impedance values of the forced-case one, associated to a forced problem. The comparison between the LSA results and the impedance predictions at $\mathcal{O}(\epsilon^1)$ are presented in Fig. 9, showing the λ_r predictions as function of U^* .

Firstly, comparison is made for two different values of U^* and for a value of $m^* \gg 1$. Fig. 9(a) shows a good agreement, not just at $\mathcal{O}(\epsilon^0)$, i.e., for $\lambda_r \rightarrow 0$, but also for the vicinity values. However, as the Re approaches the critical value of $Re_{c3} = 47$, the impedance-based results seem to deviate from the LSA results, namely for important values of λ_r . This could be explained by the fact that, as one approaches Re_{c3} , the modes become coupled $\forall m^*$. This observation can more clearly be seen in Fig. 9(b), where the Re is fixed ($Re = 40$) and m^* varies. In this case, for $m^* \gg 1$, a good agreement at $\mathcal{O}(\epsilon^0)$ and $\mathcal{O}(\epsilon^1)$ is observed, as before. However, as m^* decreases, the predictions at $\mathcal{O}(\epsilon^1)$ start to disagree with the LSA results. Moreover, one can see that the impedance results tend to “jump” to the FM, crossing $\lambda_r = 0$ where no values of U^* should exist.

5.8. Damping Factor Effect

Until now, all the discussion was made by supposing $\gamma = 0$. This assumption will intuitively set the amplification rate of the eigenmodes to their highest values, i.e. for the same set of (Re, m^*, U^*) values, the most linearly unstable mode will be the one with $\gamma = 0$. Any value of γ different from zero will damp the system and render it “more stable”.

The goal was to investigate the effect of the damp-

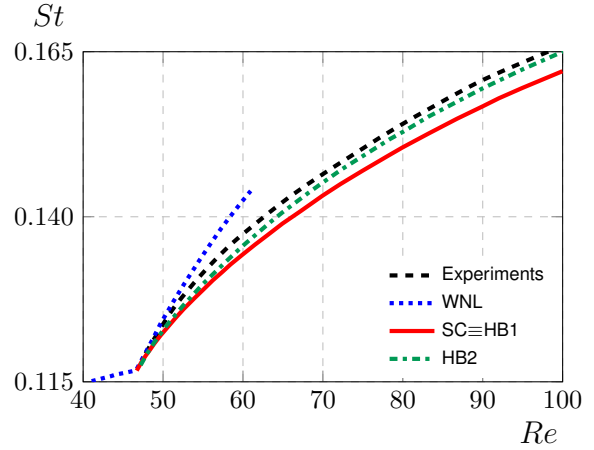
ing factor on the first instability threshold, Re_{c1} . It was found a relation between the product γm^* and the Re_{c1} for $m^* \gg 1$. This relation is sketched in Fig. 10 for several mass ratios. One can firstly notice that, for $\gamma = 0$, all the curves converge to the Re_{c1} discussed in the previous paragraphs. Secondly, for high values of γ (or γm^*), the threshold will tend to a different value of Re , depending on the mass ratio, in a similar way as the one expected in Sec. 5.6. For $m^* \gg 1$, the threshold will tend to the value of the fixed-case cylinder, i.e. $Re_{c1} \rightarrow Re_{c3}$. As the mass ratio decreases, the asymptotic value of Re_{c1} also decreases until reach the value of Re_{c2} for $m^* \ll 1$, i.e. $Re_{c1} \rightarrow Re_{c2}$. In conclusion, it can be said that the damping removes energy from the system, triggering the instability at a higher Re .

6. Non-Linear Analysis

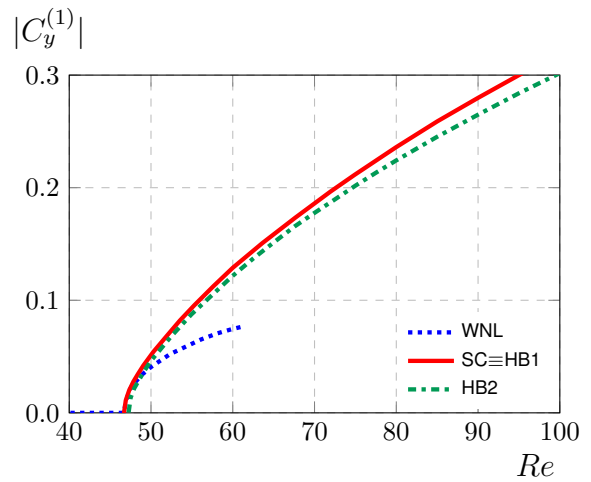
As discussed in the Introduction, the main goal of a non-linear analysis is to characterise the amplitude of the oscillation during the transition phase to the limit cycle and to describe the properties of such limit cycle in terms of amplitude and frequency. Therefore, the pertinence of the non-linear analysis lies on a Re regime above the threshold, where the steady state solution is no longer stable. For the fixed-case cylinder, this clearly means $Re > Re_{c3} \equiv Re_c$, whereas for the free-case cylinder, it will depend on the damping factor, mass ratio and reduced velocity parameters.

6.1. Weakly Non-Linear and Self-Consistent Approaches

A first analysis was made considering the fixed-case cylinder. The results of the WNL and SC approaches for the St and $|C_y^{(1)}|$ (fundamental frequency contribution on the vertical force coefficient) as function of Re are depicted in Fig. 11. Additionally, the results for the 1st and 2nd orders HB approach (HB1 and HB2) are also presented. Regarding the WNL results, they give a good prediction near Re_c when compared with the experiments from [12]. However, a significant deviation appears very rapidly and disagreement is relatively large at $Re = 60$. When comparing the other quantities, as the energy-amplitude (defined as the square-root of the phase averaged kinetic energy associated to the non-linear perturbation), disagreement is present as low as $Re = 48$. This is because the asymptotic hierarchy of the WNL equations becomes invalid when the amplitude of the disturbances becomes large enough for non-linearities to set in. In contrast, the SC results show a good agreement in the Re range considered, both for the St and the $|C_y^{(1)}|$, when compared with the experiments and the HB results. This is a direct consequence of the lack of such asymptotic hierarchy in the SC model, where the fluctuation is built as a first-order correction of the leading eigenmode



(a) St variation with Re .



(b) $|C_y^{(1)}|$ variation with Re .

Figure 11: Variation of St and $|C_y^{(1)}|$ for three different non-linear approaches. The dashed black line corresponds to the experiments from [12].

of the mean flow, and all effects are encompassed rigorously regardless of their order of magnitude.

Having these results in mind, a WNL approach for the free-case cylinder does not seem relevant, since results diverge rapidly as Re increases. However, a SC approach is of interest, as the results for the fixed-case match the experiments made in a wider Re range. A clever idea, if one is only interested in the limit cycle, would be to directly use a HB approach.

6.2. Harmonic Balance Approach

The purpose of the HB approach is only to characterise the limit cycle of the cylinder's wake. Consequently, the transition features of the SC method are avoided, gaining a considerable amount of time. Once this limit cycle is achieved in the SC approach, the SC and HB1 results will coincide. Further, to confirm the predominance of the fundamental harmonic in the present case, the 2nd Order HB results

were also plotted in Fig. 11. As seen in Fig. 11(a), the HB2 results show the best agreement with [12] in the Re range considered.

When comparing results from HB1 and HB2, one can see that the cylinder's wake is mainly governed by the fundamental frequency, although HB2 results are closer to the experiments, as expected. This is not the case, for example, in a flow over a cavity, where the contribution of the second harmonic is non negligible. Furthermore, the SC method has been expanded to the second and even third orders in [13], corresponding always to the respective order of the HB approaches when the limit cycle is reached.

The 1st order HB approach was implemented in the free-case problem. Nevertheless, no cylinder motion was captured, as it would be expected. It is expected that a higher order HB approach is needed, in order to well characterise the wake and the cylinder's behaviour.

6.3. Truncation Order of the HB Approach

Caution should be used when generalising the present method to other cases involving significant generation of higher harmonics. The above discussed case of the cavity is one example where a 1st order HB is not sufficient to correctly characterise the fluid properties of the problem. The anticipation of the proper number of harmonics to be retained can be achieved by resorting to a Fast Fourier Transform (FFT) to extract the structure of the various harmonics (see, for instance, [13], §6.2).

7. Conclusions and Future Work

A first threshold associated to the asymmetrical vortex detachment and therefore to the onset of the cylinder's motion has found to exist as low as $Re \approx 20$ via a global LSA, depending on the (m^*, U^*, γ) parameters of the free spring system. In particular, the parameter γ was found to be associated to an increase of the Re value at which the first threshold appears.

In the non-linear fixed-case cylinder, the HB approach revealed to be the faster and most accurate non-linear approach. The decomposition of the state solution based on a Fourier Series, enabled to directly characterise the limit cycle above the critical Re_c , having a important gain in time and simplicity of computation.

As future work, the addition of the horizontal displacement is expected to decrease even further the Re_c in a LSA frame. Concomitantly, an extension of the impedance-based predictions to coupled mode configurations and to damping factors different from zero has also an interest of being investigated, due to the time computation saved (associated to a forced-case problem). Regarding the non-linear approach, a practical extension of the HB method to a higher harmonic order for the free-case cylinder is expected

to reveal new branches in the $|\zeta| - U^*$ plane.

References

- [1] B. R. Noack and H. Eckelmann. A global stability analysis of the steady and periodic cylinder. *J. Fluid Mech.*, 270:297–330, 1994.
- [2] C. Cossu and L. Morino. On the instability of a spring-mounted circular cylinder in a viscous flow at low reynolds numbers. *J. Fluids Struct.*, 14:183–196, 2000.
- [3] P. Meliga and J. M. Chomaz. An asymptotic expansion for the vortex-induced vibrations of a circular cylinder. *J. Fluid Mech.*, 671:137–167, 2011.
- [4] W. Zhang, X. Li, Z. Ye, and Y. Jiang. Mechanism of frequency lock-in in vortex-induced vibrations at low reynolds numbers. *J. Fluid Mech.*, 783:72–102, 2015.
- [5] Navrose and S. Mittal. Lock-in in vortex-induced vibration. *J. Fluid Mech.*, 794:565–594, 2016.
- [6] D. Sipp and A. Lebedev. Global stability of base and mean flows: a general approach and its applications to cylinder and open cavity flows. *J. Fluid Mech.*, 593:333–358, 2007.
- [7] V. Mantić-Lugo, C. Arratia, and F. Gallaire. A self-consistent model for the saturation dynamics of the vortex shedding around the mean flow in the unstable cylinder wake. *Phys. Fluids*, 27:074103, 2015.
- [8] F. Hecht. BAMG: Bidimensional anisotropic mesh generator. *INRIA report*, 1998.
- [9] F. Giannetti and P. Luchini. Structural sensitivity of the first instability of the cylinder wake. *J. Fluid Mech.*, 581:167–197, 2007.
- [10] J. S. Leontini. *A Numerical Investigation of Transversely-Oscillating Cylinders in Two-Dimensional Flow*. PhD thesis, Monash University, Australia, 2007.
- [11] D. Fabre, V. Citro, D. Ferreira Sabino, P. Bonnefis, and F. Giannetti. A practical review on linear and nonlinear global approaches to flow instabilities. *ASME: Appl. Phys. Rev.*, submitted, 2018.
- [12] C. H. K. Williamson and A. Roshko. Vortex formation in the wake of an oscillating cylinder. *J. Fluids Struct.*, 2:355–381, 1988.
- [13] P. Meliga. Harmonics generation and the mechanics of saturation in flow over an open cavity: a second-order self-consistent description. *J. Fluid Mech.*, 826:503–521, 2017.